OPEN ACCESS
IOP Publishing | International Atomic Energy Agency
Nuclear Fusion
Nucl. Fusion **63** (2023) 026015 (11pp)
https://doi.org/10.1088/1741-4326/acab15

Zonal flow excitation in electron-scale tokamak turbulence

Stefan Tirkas[1,*], Haotian Chen[2], Gabriele Merlo[3], Frank Jenko[4] and Scott Parker[5]

[1] University of Colorado at Boulder, Boulder, CO 80309, United States of America
[2] Southwestern Institute of Physics, Chengdu 610041, China
[3] The University of Texas at Austin, Austin, TX 78712, United States of America
[4] Max Planck Institute for Plasma Physics, Boltzmannstr 2, 85748 Garching, Germany
[5] Renewable and Sustainable Energy Institute, University of Colorado at Boulder, Boulder, CO 80303, United States of America

E-mail: stefan.tirkas@colorado.edu

Received 20 September 2022, revised 22 November 2022
Accepted for publication 13 December 2022
Published 3 January 2023

Abstract

The derivation of an intermediate-scale gyrokinetic-electron theory in nonuniform tokamak plasmas (Chen *et al* 2021 *Nucl. Fusion* **61** 066017) has shown that a Navier–Stokes type nonlinearity couples electron-temperature-gradient (ETG) modes and zonal flow (ZF) modes with wavelengths much shorter than the ion gyroradius but much longer than the electron gyroradius. This intermediate-scale ETG-ZF coupling is typically stronger than the Hasegawa–Mima type nonlinearity characteristic of the fluid approximation and is predicted to lead to relevant ZF generation and ETG mode regulation. Electron-scale, continuum, gyrokinetic simulation results are presented here which include both single-mode ETG and full-spectrum ETG turbulence. The ZF generation due to single ETG modes is investigated and the single-mode intermediate-scale results are found to be in agreement with theory. The full-spectrum results are then presented and explained qualitatively in terms of the single-mode results. It is found that the ETG-driven ZFs regulate intermediate-scale electron heat flux transport to levels in the predicted range.

Keywords: gyrokinetics, microinstabilities, drift waves, tokamaks

(Some figures may appear in colour only in the online journal)

1. Introduction

Electron-scale turbulence is a plausible explanation for the anomalous transport of electron energy well above the neoclassical values seen in a variety of tokamak plasma scenarios [1–4]. Additionally, electron energy transport may become more important in future burning plasma experiments such as ITER because the electron channel is preferentially heated by Coulomb collisions with fusion alpha particles. The electron-temperature-gradient (ETG) instability produces radially-elongated streamers at the electron gyroradius scale and is a primary candidate to explain electron-scale transport [2, 4–9]. Electron heat flux due to ETG turbulence has been seen to play a role in various tokamak experiments [10–13], and the inclusion of electron-scale dynamics at the ion scale has resulted in better agreement with experimental heat flux levels [14, 15].

Electron-scale [16, 17] and multiscale [14, 15] long-time, large-box gyrokinetic flux-tube simulations have reported that intermediate-scale zonal flows (ZFs) help to regulate streamer turbulence in the quasi-saturated state and can eventually

* Author to whom any correspondence should be addressed.

become dominant. These results are inconsistent with fluid ETG turbulence models in which ZF generation occurs via the standard Hasegawa–Mima nonlinear mechanism [18], which is significantly weaker for ETG turbulence than for ion-temperature-gradient (ITG) turbulence [19, 20]. Moreover, while shearing due to ZFs generated by ITG turbulence can suppress ion transport levels, the finer scale ETG turbulence is unlikely to be affected by the ITG-driven ZFs [1, 21]. These effects have led to the expectation of a streamer-dominated steady state at the electron scale.

A weak-turbulence, toroidal, gyrokinetic-electron analysis [22] of nonuniform tokamak plasmas in the intermediate-scale ($k_\perp^2\rho_e^2 \ll 1 \ll k_\perp^2\rho_i^2$) results in a Navier–Stokes type nonlinearity which is typically stronger than the Hasegawa–Mima coupling of the fluid approximation. Here $k_\perp$ is the wavenumber perpendicular to the magnetic field and ρ is the particle gyroradius. The subscripts i and e denote ions and electrons respectively. This stronger Navier–Stokes type nonlinearity is predicted to drive notable ZF generation and ETG mode regulation at intermediate scales when compared to the Hasegawa–Mima type coupling of the short-wavelength fluid regime [22].

ETG mode saturation in the short-wavelength fluid regime has been extensively studied and includes saturation mechanisms such as secondary instabilities [6, 7] and toroidal inverse-cascading [19–21] which would lead to a turbulent state characterized by intermediate-scale ETG modes. After the initial transition to the intermediate scale, the nonlinear interaction between ETG and ZF modes is expected to be enhanced such that ZFs may grow to regulate long-term steady state transport levels as measured by experiment [22]. The intermediate-scale turbulent state might then be characterized by kinetic saturation mechanisms such as standard quasilinear estimates [23–25] and $\mathbf{E}\times\mathbf{B}$ particle trapping [26].

Collisionless Cyclone base-case (CBC) simulations of ETG turbulence initially reported the algebraic growth of ZFs into late times [16]. Electron-scale (Mega Ampere Spherical Tokamak) MAST simulations [17] demonstrated that the long-time saturated electron heat flux scales roughly proportionally to the collisionality, and this was tied to the nonlinear interaction of ETG modes with ZFs which are well-known to be damped by collisions [27]. In both cases, an initial turbulent state developed characterized by ETG mode streamers which were eventually suppressed by the slow growth of intermediate-scale ZFs. DIII-D and Alcator C-Mod simulations [14, 15] involving multiscale ion and electron dynamics also saw significant intermediate-scale ZF generation which helped to suppress ITG and ETG turbulence into the late stage.

This paper provides results which compare the generation of ZFs by ETG turbulence in electron-scale, gyrokinetic simulations with theoretical predictions in the intermediate-scale limit [22]. We first provide the details of the simulation parameters in section 2. This is followed by analysis of two types of nonlinear simulations. The 'single-mode' results serve to illuminate the role of a single ETG mode in generating ZF and are covered in section 3. As the theoretical description is limited to a single ETG mode for tractability [22], these results convey the primary scope of this paper. The 'full-spectrum' nonlinear simulations provided in section 4 include a typical range of ETG modes and are qualitatively explained in terms of the single-mode results. In both types of simulations it is found that intermediate-scale ZFs are primarily driven by slowly-saturating intermediate-scale ETG modes. The results are in good agreement with the gyrokinetic theory in the intermediate-scale and the electron fluid models at the short wavelength scale.

2. Simulation model and parameters

We employ GENE [6, 28], an Eulerian 5-d gyrokinetic continuum code, in the flux-tube limit appropriate for electron-scale turbulence. Gyrokinetic ions and electrons are taken with standard CBC parameters which are typical of H-mode core plasmas, but here a simplified circular geometry is used [29–32]. First, the linear ion-scale benchmark in [32] was verified, then the simulation was converted to the electron scale by reducing the perpendicular box dimensions by a factor of $\sqrt{m_i/m_e} \sim 42$. Here, m_e is the electron mass, and m_i is the ion mass which is taken to be the proton mass, m_p. For the electron-scale case the ITG was set to zero to suppress long-wavelength ion turbulence and focus on electron-scale physics.

The mode frequencies, ω, and growth rates, γ, resulting from the linear Gyrokinetic Electromagnetic Numerical Experiment (GENE) simulations are shown as functions of $k_y\rho_i$ in figure 1 above. The frequencies are normalized to units of R/c_s, as listed with other GENE normalizations in table 1. Here, k_y is the binormal wavenumber of the GENE coordinate system, R is the tokamak major radius, and $c_s = \sqrt{T_i/m_e}$ is the ion sound speed with T_i the ion temperature. The ITG benchmark case is shown in figure 1*(a)* alongside the electron-scale ETG case in figure 1*(b)*. Ion-scale ETG results are shown in figure 1*(c)*, where the collisionless trapped-electron mode (CTEM) [33–35] is included. One can see the ITG mode in the lower $k_y\rho_i$ range of figure 1*(a)* characterized by propagation in the $\omega > 0$ ion diamagnetic drift direction. The ETG mode becomes unstable at higher $k_y\rho_i$ where ω crosses to the negative electron diamagnetic drift direction [3]. While the CTEM is expected to contribute to electron transport [1, 36–38], figure 1*(c)* shows that it is stable in the intermediate-scale range.

The reference values and radial profiles are taken as specified in [32] with reduced values of m_i and $\beta = 8\pi n_e T_e/B^2$. Here n_e and T_e are the electron density and temperature, and B is the on-axis magnetic field. $\beta = 10^{-5}$ was chosen to keep the simulation nearly electrostatic in order to avoid transport due to electromagnetic fluctuations. The safety factor, $q = rB_\phi/RB_\theta$, and magnetic shear, $\hat{s}$, profiles are given by $q(r) = 2.52(r/a)^2 - 0.16(r/a) + 0.86$ and $\hat{s} = \frac{r}{q}\frac{dq}{dr}$ [32]. B_ϕ and B_θ represent the toroidal and poloidal magnetic field components respectively. The radial flux-surface coordinate $r = 0.5a$ was chosen, where a is the tokamak minor radius. The normalized density and temperature gradient profiles, for a general profile $A(r)$, are defined as $R/L_A = -R\partial_r \ln(A(r))$, which can be calculated using the profile given in equation (2)

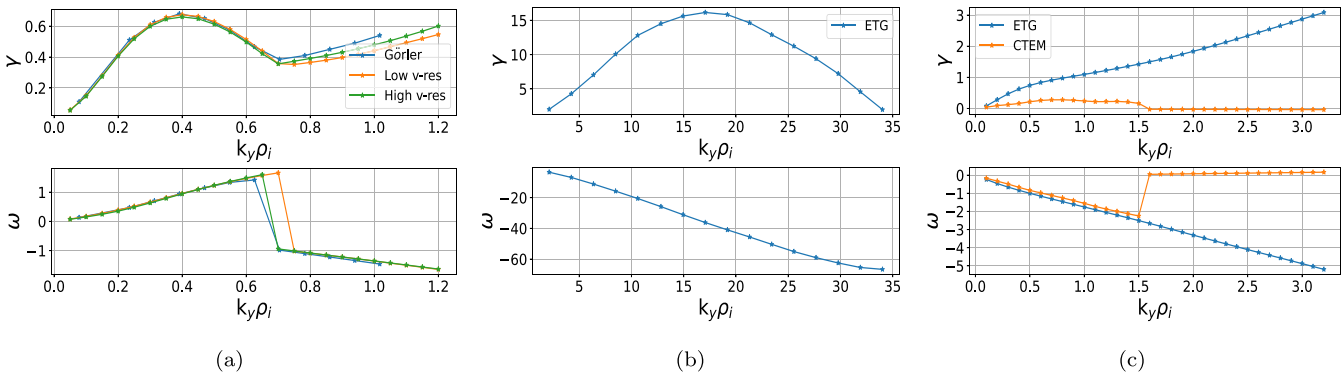

Figure 1. GENE linear simulation results showing growth rates and real mode frequencies for (*a*) CBC ITG benchmark case, (*b*) electron-scale ETG case, and (*c*) ion-scale ETG case showing CTEM modes as well. Positive(negative) frequencies indicate propagation in the ion(electron)-diamagnetic direction.

Table 1. Relevant GENE normalizations and definitions [28].

ρ^*	ρ_i/R
c_s	$\sqrt{T_i/m_e}$
t	R/c_s
ω	c_s/R
γ	c_s/R
Q_{gB}	$c_s n_e T_e (\rho^*)^2$
χ_{gB}	$\rho_i^2 c_s/R$
ϕ	$e\phi/(T_e\rho^*)$
ν_c	$\pi \ln\Lambda e^4 n_e R/(2^{3/2}T_e^2)$
Λ	$24 - \ln(\sqrt{10^{13}\cdot n_e}/(10^3 T_e))$

Table 2. GENE simulation parameters.

R(m)	1.67
$n_{i,e}(10^{19}\mathrm{m}^{-3})$	4.66
$T_{i,e}$(keV)	2.14
B_ϕ(T)	2.0
r/a	0.5
a/R	0.36
ρ^*	0.001413
β	1e−4
m_i/m_p	1.0
m_e/m_i	5.4462e−4
R/L_{T_i}	0
R/L_{T_e}	6.96
$R/L_{n_{i,e}}$	2.22
q	1.41
$\hat{s}$	0.837
ν_{ei}	0.106875

of [32]. The values of the pertinent simulation parameters are listed in table 2.

For the linear ITG case, the grid resolution was taken with 32 grid points in the radial dimension, x, and 16 grid points in the parallel spatial dimension, z. The GENE radial coordinate x corresponds to the flux-surface coordinate r for the case of a circular geometry. In figure 1*(a)* the flux-tube GENE benchmark result from [32] is marked as 'Górler' and the corresponding 'low' (32×8) and 'high' (64×16) velocity grid ($v_\parallel \times \mu$) resolution simulations have been plotted collectively. There is good agreement with the benchmark case in the ITG range. The intermediate scale is well resolved in the 'low v-res' case, and the same grid resolution was used for the nonlinear simulation, but with the radial grid resolution increased to 192 gridpoints. The perpendicular box size was reduced from $125\rho_i \times 125\rho_i$ at the ITG turbulence scale to $6\rho_i \times 3\rho_i$ at the ETG turbulence scale, where the original radial extent of the flux-tube domain was increased from $3\rho_i$ to $6\rho_i$ to allow for the full formation of the ETG mode streamers.

The electrostatic portion of the radial heat flux, $\langle Q_{ES}\rangle$, for electrons is shown approaching a statistically steady state in time in figure 2*(a)* for the collisionless, $6\rho_i \times 3\rho_i$, nonlinear, full-spectrum, electron-scale case. The heat flux is normalized to Q_{gB}, the gyroBohm normalization given in table 1, and the angled brackets, $\langle\ldots\rangle$, denote a flux-tube volume average. The heat flux is determined in GENE as [28],

$$Q_{\mathrm{ES}} = \int d^3v \left(\frac{1}{2}mv^2\right) \boldsymbol{v}_{E\times B}\cdot\hat{\mathbf{r}}\,\delta f\ , \qquad (1)$$

where δf is the distribution function perturbation, $\boldsymbol{v}_{E\times B} = -(\nabla\phi\times\boldsymbol{B})/B^2$ is the $\boldsymbol{E}\times\boldsymbol{B}$ drift, ϕ is the electrostatic potential perturbation, and m and v are the particle mass and velocity. The normalization for ϕ is given in table 1. One can see the shift from the early, nonlinear state characterized by radially-elongated electrostatic potential streamers in figure 2*(b)* to the later state of figure 2*(c)* where ZFs have become dominant. It is during this phase that intermediate-scale ZFs grow slowly into the final quasi-saturated state.

The initial condition for ϕ was realistically peaked about the most unstable mode as shown in figure 3*(a)*. This allowed for a transition from the high-k_y ETG turbulence regime to the intermediate scale where ZF generation is expected to be stronger [22]. Such ZF generation is not present in toroidal electron fluid theories [19, 20]. An inverse-cascade can clearly be seen between figures 3*(a)* and *(b)*. This initial saturation is discussed further for the single-mode simulation results presented in section 3.2, and for the well-converged, collisional, full-spectrum simulation results presented in section 4. The convergence tests for finding an optimal nonlinear box size are detailed in the appendix.

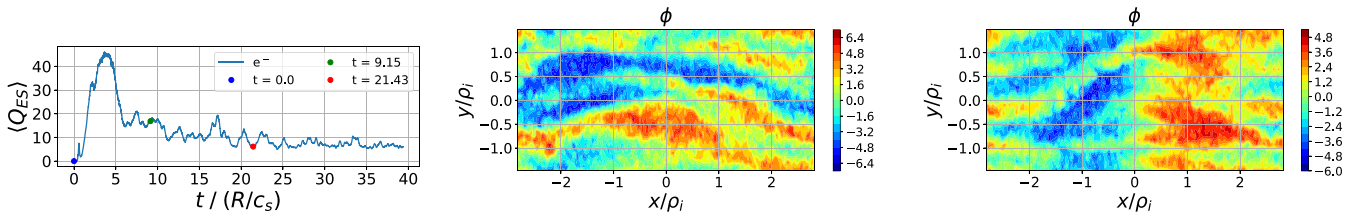

Figure 2. Original (small-box, no collisions) nonlinear simulation results showing (*a*) time-marked electrostatic electron heat flux and electrostatic potential contours for the (*b*) early nonlinear phase (green marker), and (*c*) late zonal phase (red marker).

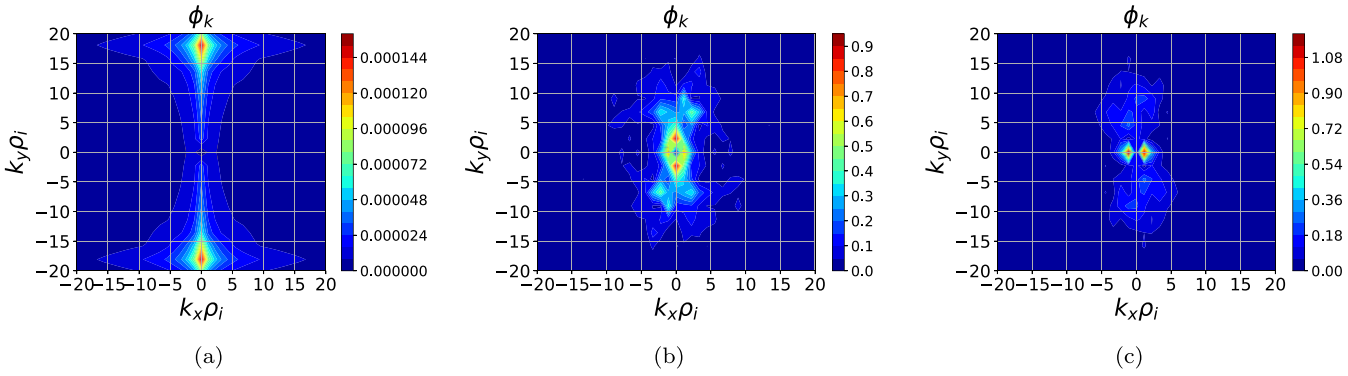

Figure 3. Original (small-box, no collisions) nonlinear simulation results showing Fourier-space electrostatic potential contours for the (*a*) initial time (blue marker), (*b*) early nonlinear phase (green marker), and (*c*) late zonal phase (red marker). The markers correspond to the times marked in figure 2*(a)*.

3. Single-mode analysis

3.1. Zonal flow generation mechanism

It was shown theoretically in [22] that intermediate-scale ZF may play a role in the nonlinear saturation of ETG turbulence in tokamak plasmas. The equations of [22] are briefly reviewed here, and the nonlinear single-mode simulation results are then presented in section 3.2 with comparison to the theory. The theoretical model takes the standard gyrokinetic equation [39] for electrons and the quasineutrality condition in the intermediate-scale limit $k_\perp^2\rho_e^2 \ll 1 \ll k_\perp^2\rho_i^2$. For long-wavelength ETG modes, one can generally assume that the growth rate is much smaller than the real frequency, $|\gamma/\omega| \ll 1$, which allows for a weak-turbulence analysis. These modes also satisfy the relation $|\omega_d| \ll |\omega|, |\omega_t|$, for ω_t and ω_d the transit and magnetic drift frequencies respectively. Local approximations [40] are then assumed for ω_d and ω_t in formulating a kinetic electron model.

The evolution of a single ETG mode can then be derived in terms of a nonlinear Schrodinger equation (NLSE) [22],

$$[i(\partial_t - \gamma_n) - b_n k_\theta^2\rho_e^2\hat{s}^2\theta_k^2 - \frac{c_n}{k_\theta^2\rho_e^2\hat{s}^2}\frac{\partial^2}{\partial\theta_k^2}]A_n(\theta_k) = \frac{-ik_\theta\rho_e\hat{s}}{\sqrt{2\pi}}\int d\vartheta_k\vartheta_k A_z(\vartheta_k)A_n(\theta_k-\vartheta_k), \quad (2)$$

with A_z and A_n the amplitudes of the ZF and ETG modes, γ_n the ETG mode growth rate, θ_k and ϑ_k the tilting angle (defined by $\theta_k = k_x/(k_y\hat{s})$) in the flux-tube limit [41] for k_y of the ETG mode), k_θ the poloidal wavenumber, and the terms including b_n and c_n coming from the frequency mismatch and plasma nonuniformity corrections respectively. b_n and c_n are specifically associated with the linear ETG dynamics as explained in [22]. The nonlinear term under the integral in equation (2) describes a Navier–Stokes type coupling due to $\mathbf{E}\times\mathbf{B}$ shearing effects. This coupling is $\mathcal{O}((k_\theta\rho_e)^{-2})$ stronger than the usual Hasegawa–Mima type coupling in the fluid limit [19, 20]. This stronger coupling results in a stronger regulation of ETG turbulence by zonal flows and also leads to a reduced threshold for ZF excitation by intermediate-scale ETG modes. The threshold condition is described further in equation (4).

The description of ZF dynamics is given by the equation [22],

$$[\partial_t + \gamma_z(1 + d_z k_\theta^2\rho_e^2 s^2\theta_k^2)]\chi_z A_z(\theta_k) = \sqrt{\frac{\pi}{2}}(k_\theta\rho_e s)\theta_k\int d\vartheta_k\vartheta_k^2[A_n(\vartheta_k)A_n^*(\vartheta_k-\theta_k)a_n^* - A_n(\vartheta_k+\theta_k)A_n^*(\vartheta_k)a_n]. \quad (3)$$

The nonlinear term under the integral in equation (3) is related to the Reynolds stress of the ETG modes. The ZF damping rate is given by $\gamma_z \simeq 3\nu_{ee}/(|\omega_{*e}|\sqrt{\epsilon})$, with ν_{ee} the electron–electron collision frequency and ω_{*e} the electron diamagnetic drift frequency. The total electric susceptibility is defined as $\chi_z = \tau + (1 + 1.6q^2/\sqrt{\epsilon})k_\theta^2\rho_e^2 s^2\theta_k^2/2$ with $\tau = T_e/T_i$. The d_z term in equation (3) represents a gyrodiffusive correction which helps suppress short wavelength ZFs [42].

The a_n term describes the parallel correlation of the ETG turbulence and is defined as $a_n(\theta_k,\vartheta_k) = \int d\eta \langle \tilde{\Phi}_n^*(\eta,\vartheta_k) v_\perp^2 \delta\tilde{H}_n(\eta,\vartheta_k+\theta_k)\rangle_v$, where η is the extended poloidal angle. Here, $\delta\tilde{H}_n$, is the non-adiabatic part of the distribution function perturbation. Keeping a_n non-local in tilting angle in order to take into account ballooning effects leads to a parallel decoupling of ETG modes and therefore ZFs as well, where $a_n = a_n(0,0)\exp(-\theta_k^2/2\bar{\eta}^2)$ for $\bar{\eta} = (\int d\eta \tilde{\Phi}^* \eta^2 \tilde{\Phi})^{1/2}$ the parallel-mode-averaged potential [22].

Equations (2) and (3) are taken together as the NLSE model. The numerical solution of the NLSE model with a single ETG mode and a range of ZF modes gives an evolution of ETG and ZF modes that can be described by three specific stages [22]. The initial stage involves uninhibited exponential growth of the ETG mode to a threshold point at which the radial beating of the ETG drives ZF growth as described by equation (3). As the ZF modes grow, they lead to radial dispersion of the initial ETG wave packet and the creation of sidebands. These sidebands then drive more ZFs via a modulational instability in the second stage. Once the ZF grows to appreciable levels in comparison with the ETG mode, the nonlinear interaction in equation (2) acts to saturate the ETG mode. In the final stage, the linear growth rate of the ETG mode becomes negligible and the NLSE model then results in slow, algebraic growth for the ZF [22]. This slow growth has been observed in previous gyrokinetic electron-scale simulations [16, 17].

A threshold condition for the ZF excitation can be calculated analytically [22] by considering a simple four-wave model for a single ZF mode, an ETG pump mode, and two ETG sideband modes. Narrow-band, rectangular functions are used to describe the ZF and ETG modes, $A_z\Pi[(\theta_k-\theta_z)/W]$ and $A_0\Pi(\theta_k/W) + A_+\Pi[(\theta_k-\theta_z)/W] + A_-\Pi[(\theta_k+\theta_z)/W]$ respectively. Here W is the full-width of the modes, θ_z is the ZF wavenumber in terms of tilting angle, and A_z,A_0, and $A_\pm$ are the ZF, ETG pump, and ETG sideband mode amplitudes. Substituting these functions into equations (2) and (3) with the assumption of no plasma nonuniformities ($c_n = 0$) and a steady state pump amplitude for simplicity, one obtains the critical threshold condition [22],

$$W^2|A_{0,c}^2| = \frac{(\Delta^2+\gamma_s^2)\gamma_z(1+d_z(k_\theta\rho_e\hat{s}\theta_z)^2)\chi_z}{(k_\theta\rho_e\hat{s}\theta_z)^4[\gamma_s \mathrm{Re}(a_n) + \Delta \mathrm{Im}(a_n)]}. \tag{4}$$

Here, $\Delta = \mathrm{Re}(b_n)(k_\theta\hat{s}\theta_z\rho_e)^2$ represents the frequency mismatch of the pump and sidebands, and $\gamma_s = \gamma_n + \mathrm{Im}(b_n)(k_\theta\hat{s}\theta_z\rho_e)^2$ is the growth rate of the sidebands. This threshold condition for ZF excitation by intermediate-scale ETG modes is $\mathcal{O}(k_\theta^2\rho_e^2)$ lower than the condition found in the fluid approximation [20], which would then lead to more effective ZF generation at intermediate scales.

The ZF modes are initially excited in a range of θ_z values. As the system evolves to the quasi-saturated state and the ETG mode is suppressed, the ZF spectrum narrows towards the most easily driven mode. Comparing the exponential θ_k dependence of the a_n term to the algebraic form of the d_z term, one finds that the parallel decoupling is largely responsible for minimizing the intermediate-scale threshold condition at low θ_z. If one considers the temporal evolution of the four-wave model, a fixed-point solution can be found with constant A_z and sufficiently low ZF damping rate, where the ZF and ETG mode amplitudes are given as [22],

$$W^2|A_{z,p}|^2 = \frac{\pi(\delta^2 - \Delta\delta - \gamma_n\gamma_s)}{(k_\theta\hat{s}\theta_z\rho_e)^2}, \tag{5}$$

and,

$$W^2|A_{0,p}|^2 = \frac{\chi_z\gamma_z(1+d_zk_\theta^2\hat{s}^2\theta_z^2\rho_e^2)[\gamma_s^2+(\delta-\Delta)^2]}{(k_\theta\hat{s}\theta_z\rho_e)^4[(\Delta-\delta)\mathrm{Im}(a_n)+\gamma_s\mathrm{Re}(a_n)]}. \tag{6}$$

Here, $\delta = \Delta\gamma_n/(\gamma_s+\gamma_n)$ represents the amplitude oscillation frequency of ETG modes due to the nonlinear ETG-ZF coupling. The single ETG mode spectrum then continues to fluctuate in k_x while the ZF mode reaches a constant, steady state [22]. Additionally, $|A_{0,p}|^2$ is then proportional to γ_z in the saturated state, and therefore the collision frequency, while $|A_{z,p}|^2$ is not. While these saturation estimates are only valid for a single ZF mode, as the ETG turbulence saturates and the ZF spectrum narrows due to the threshold condition, θ_z of the most optimally-driven mode can be used to estimate the ETG saturation level.

3.2. Single-mode simulation results

We now compare the NLSE model (equations (2) and (3)) to gyrokinetic simulation results. Collisionless, nonlinear, ETG simulations were carried out where a single unstable ETG mode ($k_x = 0$) and all ZF modes ($k_y = 0$) are retained. This fairly accurately describes the dynamics of the NLSE model. All results presented in this section are averaged over z. The ETG growth rate spectrum with respect to $k_y\rho_i$ can be utilized here to illustrate the NLSE model dynamics. As seen in figure 1*(b)*, the ETG growth rate spectrum is symmetric around the most unstable mode, so one can choose to compare the evolution of a pair of ETG modes with similar growth rates, where one mode has a $k_y\rho_i$ value in the intermediate-scale range and the other mode has a larger $k_y\rho_i$ value outside of that range. Then the ZF drive of the two modes can be compared to verify the expectations from the NLSE model.

The $k_y\rho_i = 6.36$ mode with a growth rate of $\gamma \approx 7.037$ and the $k_y\rho_i = 30$ mode with a similar growth rate of $\gamma \approx 7.015$ are taken here for comparison. Figure 4*(a)* shows the time evolution of the $k_y\rho_i = 6.36$ mode, while figure 4*(b)* shows the time evolution of the $k_y\rho_i = 30$ mode. Figure 4*(c)* shows the time evolution of the four strongest ZF modes at the final time step for the intermediate-scale case, whereas figure 4*(d)* shows a large range of ZF modes excited in the high-k_y case in order to illustrate a difference in the ZF response between the two cases. One can see that initially both ETG modes grow exponentially at similar rates until a threshold is reached, at which point ZFs are excited. For the intermediate-scale ETG mode, this phase is followed by an algebraically-growing long

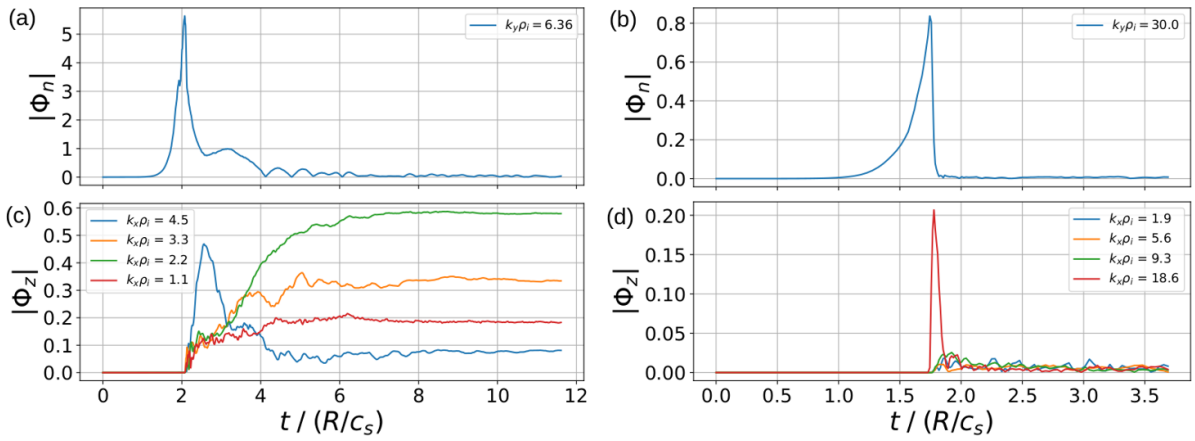

Figure 4. Plots of collisionless single ETG mode evolution for (*a*) $k_y\rho_i = 6.36$ and (*b*) $k_y\rho_i = 30$ with respective growth rates $\gamma \approx 7.037$ and 7.015. The strongest four ZF modes in the late time are plotted for (*c*) the $k_y\rho_i = 6.36$ case, while (*d*) shows the excitation of a larger range of ZF modes in the $k_y\rho_i = 30$ case.

wavelength ZF phase in which the ZF modes gradually reach a steady state value. The high-k_y results show no slowly-growing ZF phase at late times. This difference in ZF generation in the late stage is consistent with the threshold condition given in equation (4). The intermediate-scale ETG mode continues to slowly drive ZFs as it is suppressed to lower levels, whereas the high-k_y ETG mode does not.

The peak level of the ETG mode is much lower for the high-k_y case than for the intermediate-scale case. This result is not expected from the NLSE model as the shearing of the ETG mode by the wave-wave coupling should be stronger in the intermediate scale than at higher k_y. ZFs are also generated earlier in the high-k_y case, indicating a lower threshold initially, which is inconsistent with the NLSE model. One noticeable difference between the single-mode GENE simulations and the NLSE model is that the NLSE model only includes the ZF shearing suppression mechanism, whereas the single-mode GENE simulations include other saturation mechanisms. Comparing the zonal response between the two cases, it is found that the initial ZF excitation shown in figure 4*(d)* is much more abrupt, possibly indicative of a secondary instability [6, 7, 43]. The change in ETG-ZF dynamics in the single-mode results is found to occur near $k_y\rho_i \sim 15$. This difference in behavior likely indicates the reason for the transition to the intermediate scale mentioned previously in section 2, and this is further discussed in comparison to the full-spectrum simulation results presented in section 4.

Figure 5 shows the sum of all ZF mode amplitudes, $\sum|\phi_z|$, as a function of $k_y\rho_i$. Each value of $k_y\rho_i$ represents initializing with a different unstable ETG mode. The sum is taken at the final simulation time, where the ZF mode amplitudes are nearing steady state levels. The notable region of ZF generation is clearly seen to be in the intermediate-scale range, as expected by the NLSE model. Shorter ETG mode wavelengths correspond to weaker ZFs at late times, in agreement with fluid ETG models. In addition, the drop-off at long ETG mode wavelengths is reasonable due to trapped electron effects at this wavenumber range [44]. A validation of this

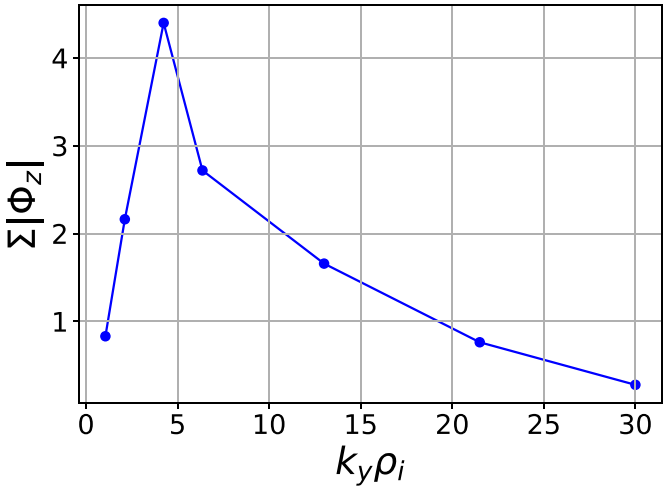

Figure 5. Plot of the sum of zonal potential amplitudes at final times, $\sum|\phi_z| = \sum_{k_x}|\phi_{k_x,0}|$, as driven by a single ETG mode. The fourth and seventh points correspond to the ETG modes from figure 4.

expectation for the full-spectrum simulations is provided in the appendix.

The unstable ETG mode is shown to be suppressed at late times in figures 4*(a)* and *(b)*. The total amplitude, $\langle|\phi|\rangle = (\int d\theta_k|\phi_k|^2)^{1/2}$, of the ETG mode is small in comparison to the ZF amplitude. In contrast, the NLSE model simulation results given in figure 3 of [22] show that the total ETG and ZF mode amplitudes, $\langle|\phi|\rangle$, are of similar strength and fluctuating in the late stage. One reason to expect the strong ETG suppression in the gyrokinetic simulations is the lack of collisionality which would damp the ZF due to the collisional dependence of the γ_z term in equation (3). Additionally, the NLSE model assumes a Gaussian radial spectrum for the ETG mode, while the single-mode flux-tube GENE simulations take $k_x = 0$ initially. The globally-Gaussian radial distribution of the ballooning modes would lead to more radial ETG mode overlap, which would then drive more ZF generation as predicted by equation (3).

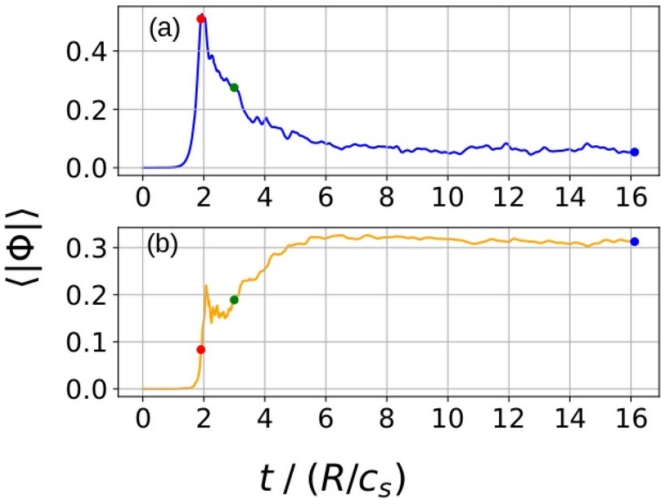

Figure 6. Plot of total (*a*) ETG and (*b*) ZF mode potential as an integral over k_x in the collisional, Gaussian-k_x ETG case for $k_y\rho_i = 6.36$. Markers have been added to match the spectral snapshots of figure 7.

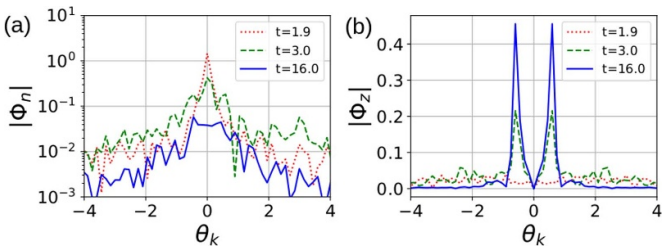

Figure 7. Radial-spectrum snapshots of (*a*) the single ETG mode and (*b*) ZF as a function of tilting angle for the $k_y\rho_i = 6.36$ case. Snapshot times match the markers in figure 6.

We were able to obtain more physical results for the $k_y\rho_i = 6.36$ case in which the ETG and ZF modes fluctuate about similar steady state values due to their nonlinear coupling. These results were achieved by including the physical collisionality taken in section 4, such that $\gamma_z = 0.014$, and by initializing the ETG mode with a Gaussian k_x and z spectrum such that $\phi(k_x, z, t = 0) \sim e^{-(k_x^2+z^2)/8\pi^2}$. The corresponding $\langle|\phi|\rangle$ for the ETG and ZF modes are plotted in figure 6. One can see the strong drive of the ZF, as well as the late-stage fluctuations of both ETG and ZF modes. Figure 7 shows that over time the Gaussian radial spectrum of the ETG mode is broadening into sidebands, while the radial spectrum of the ZF modes narrows from a broad distribution to a peak at a final, low-θ_z mode number, as predicted by the NLSE model [22]. These results suggest that one should perform global simulations to see results most consistent with the NLSE model.

The improved single-mode results for the $k_y\rho_i = 6.36$ case showed large θ_k-averaged fluctuations for the ETG mode compared to more fixed ZF fluctuations. These results agree with the expectations of equations (5) and (6). The fluctuations can be seen in figure 8, where the average dimensionless radial wavenumber, $\langle|\theta_k|\rangle = \left(\int d\theta_k \theta_k^2 |\phi_k|^2\right)^{1/2} / \langle|\phi_k|\rangle$, is plotted for the ETG and ZF modes respectively. The ratio of the total absolute amplitude of ZF to ETG modes is given in figure 9 as

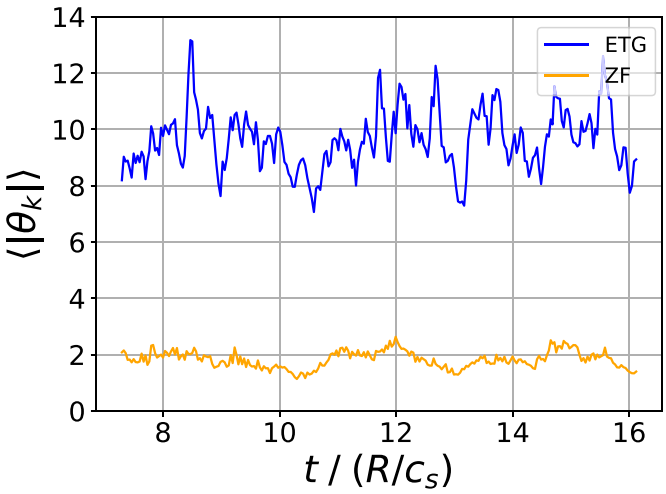

Figure 8. Plot in time of the average dimensionless radial wavenumber for the total ETG and ZF spectra in the quasi-saturated stage.

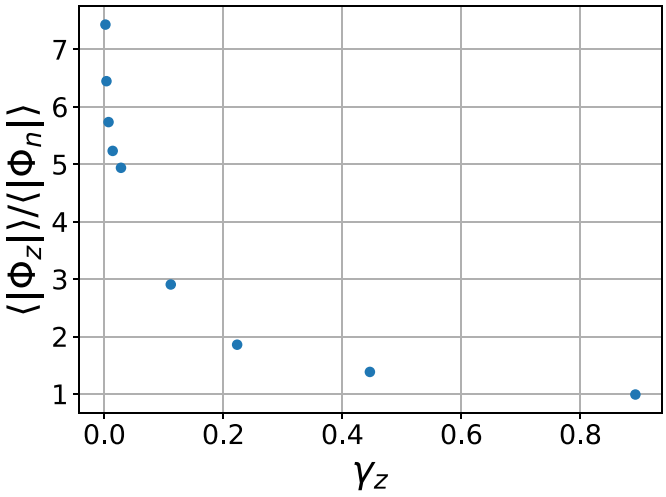

Figure 9. Ratio of total absolute amplitudes of ZF to ETG modes with varying collisionality. Results are taken at the final timestep. The reference value corresponds to the fourth point, $\gamma_z = 0.014$.

a function of γ_z and is consistent with the trend from the NLSE model. The late-stage behavior of the ETG and ZF k_x-spectra, as shown in figures 7 and 8, and the collisional behavior of the mode amplitude ratio agree well with the late-time behavior reported in the electron-scale MAST simulations of [17].

4. Full-spectrum simulation results

The full-spectrum nonlinear simulation results are presented here and the intermediate-scale ZF generation mechanism is further investigated. Including multiple toroidal modes results in a final quasi-saturated heat flux characterized by richer turbulent interactions. Figure 10*(a)* shows the time history of the heat flux for the well-converged $24\rho_i \times 3\rho_i$ case with collisionality. The four strongest ZF modes at the final time are presented in figure 10(*b*). The value of the normalized electron–ion collision frequency used is $\nu_{ei} = 0.106875$. This frequency is

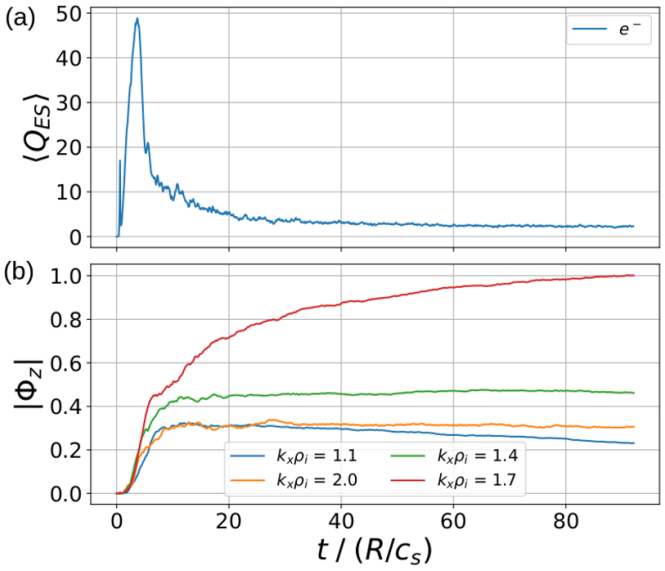

Figure 10. Full-spectrum collisional nonlinear simulation results showing (*a*) the electron heat flux time-evolution and (*b*) the time evolution of the four strongest final ZF modes. Data is averaged over z.

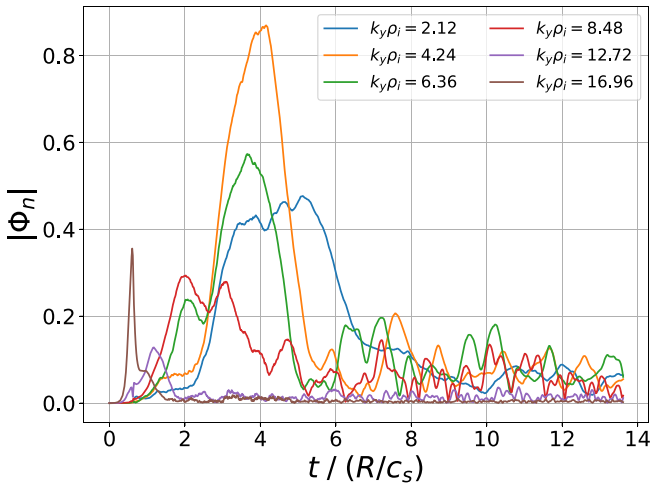

Figure 11. Time trace of full-spectrum ETG modes ranging from the longest mode to the most unstable mode. Data is averaged over z.

defined as $\nu_{ei} = 4v_{te}\nu_c/R$, where $v_{te} = \sqrt{T_e/m_e}$ and ν_c is the collision frequency given in table 1. The self-adjoint form of the standard Landau–Boltzmann collision operator is used. Realistic collisionality allows for ZF damping when reaching a final state, and the simulation was carried out to a sufficiently long non-dimensional time, $t/(R/c_s) = 90$, to ensure that a quasi-saturated steady state in $\langle Q_{\rm ES} \rangle$ is achieved. The convergence with respect to box size is discussed in the appendix.

Figure 11 shows the evolution of various ETG modes ranging from the longest wavelength to the most unstable mode. The shorter wavelength modes saturate very quickly to negligible levels, in agreement with the single-mode results, and are

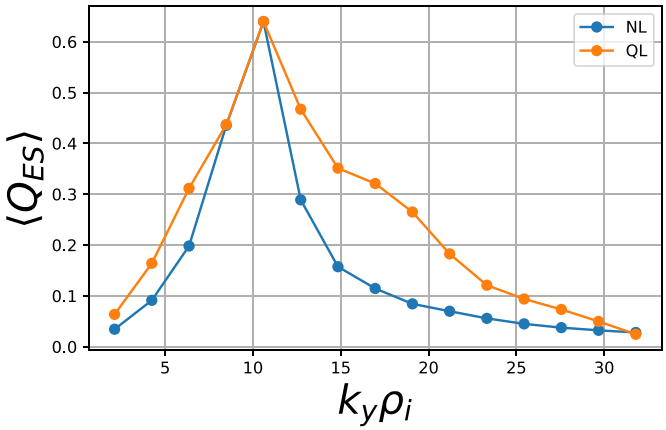

Figure 12. Comparison of quasilinear and nonlinear heat flux spectra for the $24\rho_i \times 3\rho_i$ full-spectrum electron-scale case. NL and QL stand for nonlinear and quasilinear respectively.

omitted. One can observe that the intermediate-scale modes saturate the slowest and reach the highest levels. During the period of intermediate-scale ETG mode growth, the ZF modes shown in figure 10(*b*) are driven exponentially by the radial beating of ETG modes, as well as by the modulational instability. Once the ETG modes reach a quasi-saturated state, the ZF modes continue to grow slowly in agreement with the single-mode simulation results. Considering the findings of the NLSE model, the single-mode simulations results of section 3.2, and the full-spectrum simulation results discussed here, it is the intermediate-scale ETG modes which are most responsible for driving ZF mode growth into the late stage.

The heat flux spectrum for the full-spectrum case is shown in figure 12, alongside a quasilinear saturation estimate. The quasilinear estimate of the heat flux for a single k_y mode is calculated as [45, 46],

$$Q^{QL}_{k_y} = A_0 \frac{(\gamma/\langle k^2_\perp \rangle)^2}{|\phi_{0,k_y}(0)|^2} Q^{\rm lin.}_{k_y}, \tag{7}$$

with $Q^{\rm lin.}_{k_y}$ representing the linear simulation results for the heat flux and $\phi_{0,k_y}(0)$ the linear electrostatic potential at $k_x = z = 0$. A_0 represents a constant of proportionality, and $\langle k^2_\perp \rangle$ is the ballooning-angle-averaged perpendicular wavenumber, defined as [46],

$$\langle k^2_\perp \rangle = \frac{\sum_{k_x} \int (g^{xx}k^2_x + 2g^{xy}k_xk_y + g^{yy}k^2_y)|\phi_k(z)|^2 dz}{\sum_{k_x} \int |\phi_k(z)|^2 dz}. \tag{8}$$

Here, ϕ_k represents a Fourier mode of the electrostatic potential perturbation, and $g^{\mu\nu} = \nabla\mu \cdot \nabla\nu$ gives the metric tensor coefficients of the GENE coordinate system. A sum over all k_x values was required for the drop-off of saturation levels at low $k_y\rho_i$.

This model of mode saturation describes a balance of the unstable growth of the instability with turbulent diffusion based on a mixing-length estimate [23–25], and gives notable

agreement with the nonlinear heat flux spectrum in the intermediate scale. The disparity between the quasilinear model and the nonlinear heat flux spectrum is greatest for ETG modes with wavenumbers higher than $k_y\rho_i \approx 12$. This suggests other, stronger saturation mechanisms for these modes. While new effects, such as toroidal inverse-cascading [19–21], may play a role in the full-spectrum case, the difference in the heat flux spectra also agrees with the transition in ETG-ZF dynamics found to occur around $k_y\rho_i = 15$ for the single-mode results. The more abrupt ZF response and quicker saturation of the higher k_y modes may be consistent with secondary instability theory [6, 7], where a $|\phi_n| \sim \gamma/\langle k_\perp^4 \rangle$ saturation model for ETG mode amplitudes predicts a steeper drop-off near $k_y\rho_i \approx 12$ than that of the quasilinear mixing-length estimate.

Finally, we present a comparison of turbulent and neoclassical transport levels at both ion and electron scales. Because the electron-scale case takes the ITG to zero, we can compare the electron-scale thermal diffusivity to that of the ion-scale ITG case with adiabatic electrons to understand the importance of regulation by ZFs at each scale. In units normalized to the specific species of interest, the thermal diffusion coefficients due to electrostatic turbulence are $\langle \chi_{\rm ES} \rangle_i = 0.7\rho_i^2 v_{Ti}/L_{Ti}$ for the ion-scale ITG case and $\langle \chi_{\rm ES} \rangle_e = 2.8\rho_e^2 v_{Te}/L_{Te}$ for the electron-scale ETG case, where v_{Ts} is the thermal velocity, $\sqrt{2T_s/m_s}$, for a species s. This suggests that the ETG-driven ZFs do not regulate ETG turbulence as strongly as the isomorphic counterpart ITG turbulence is regulated by ITG-driven ZFs.

The neoclassical transport values were calculated using GENE for both the ion and electron scale cases. Given in units of χ_{gB} from table 1, the neoclassical thermal diffusivities are $\langle \chi_{\rm neo} \rangle_i = 0.14\chi_{\rm gB}$ and $\langle \chi_{\rm neo} \rangle_e = 0.004\chi_{\rm gB}$. The neoclassical values are in close agreement with the theoretical expectation that $\chi_i = \sqrt{m_i/m_e}\chi_e$, and are negligible compared to the turbulent thermal diffusivities, $\langle \chi_{\rm ES} \rangle_i = 6.95\chi_{\rm gB}$ and $\langle \chi_{\rm ES} \rangle_e = 0.328\chi_{\rm gB}$. The late-time heat flux spectrum peaks in the intermediate scale at $k_y\rho_i = 10.6$ with $\langle Q_{ES} \rangle_e = 0.66Q_{\rm gB}$ and drops off to $\langle Q_{\rm ES} \rangle_e = 0.10Q_{gB}$ and $0.11Q_{gB}$ for $k_y\rho_i = 4.24$ and 16.96 respectively. These values are in good agreement with the theoretical expectation that $Q/Q_{gB} \sim \mathcal{O}(0.01) - \mathcal{O}(0.1)$ (in the units of table 1) for the intermediate-scale ETG modes [22].

5. Discussion

We have shown, using the single-mode nonlinear simulations, that the NLSE model [22] accurately describes the ZF generation mechanism by intermediate-scale ETG modes and that it provides a theoretical understanding for the slow growth of long-wavelength ZFs into the long-term quasi-saturated state. As the NLSE model considers only a single ETG mode for a practicable analysis, one cannot say conclusively that the same is true of the full-spectrum nonlinear results. However, in the full-spectrum case the high-k_y ETG modes are quickly saturated by a stronger ZF response as compared to the intermediate-scale ETG modes. The intermediate-scale ETG modes then drive exponential ZF mode growth initially, and slow, algebraic ZF mode growth as they are suppressed in the late stage. This result is in good agreement with the NLSE model for intermediate-scale ETG-ZF dynamics, as well as various long time, saturated electron-scale [16, 17] and multiscale [14, 15] flux-tube simulations.

The final transport levels for the full-spectrum case are in similar ranges found in thorough electron-scale CBC benchmarks which compare well with experimental observations [9]. As the ZFs are driven at long electron-scale wavelengths, multiscale effects could become important and ETG-driven ZFs may have an effect on ion-scale turbulence. This effect where intermediate-scale ZFs contribute to ion-scale turbulence suppression has been reported in large multiscale simulations [14, 15].

Acknowledgments

This research was supported by the SciDAC-4 project High-fidelity Boundary Plasma Simulation funded by the U.S. Department of Energy (U.S. DOE) Office of Science under Grant DE-SC-000801. Research was also carried out under U.S. DOE Grant DE-FG02-08ER54954.

Appendix. Nonlinear convergence tests

This section details a 'full-spectrum' nonlinear simulation box-size convergence study. The perpendicular box size is varied in terms of the basic $6\rho_i \times 3\rho_i$ electron-scale box size shown in figure 2. The collisionality was set to the reference value discussed in section 4. Four perpendicular domain sizes are presented: $6\rho_i \times 3\rho_i$, $12\rho_i \times 3\rho_i$, $24\rho_i \times 3\rho_i$, and $12\rho_i \times 6\rho_i$. These cases consider the importance of correctly resolving the ETG streamer lengths and the longest wavelength ZF modes. Additionally, the inclusion of longer ETG mode wavelengths is considered in the $12\rho_i \times 6\rho_i$ case to verify the findings of section 3.2. The number of radial gridpoints was increased in each simulation to retain the original resolution.

The electron heat flux for each case is shown over time in figure 13. One can clearly see that the increase in radial dimension is necessary to correctly resolve the heat flux. The late-stage ZFs of the $6\rho_i \times 3\rho_i$ case, as shown in figure 3*(c)*, are peaking at the longest mode allowable and the box size must be increased to correctly resolve the longest modes. Allowing for longer wavelength ZF modes leads to stronger regulation of the heat flux as seen in figure 13.

The time evolution of the ETG modes for the $12\rho_i \times 6\rho_i$ case is shown in figure 14*(a)*, and the time evolution of the four strongest ZF modes at the final time is shown in figure 14*(b)*. These results are qualitatively similar to the $24\rho_i \times 3\rho_i$ case shown in figures 11 and 10*(b)*. In this new case, the longest wavelength ETG mode, $k_y\rho_i = 1.06$, grows to the highest level. However, it can be seen in figure 14*(b)* that from non-dimensional times 5–10 $t/(R/c_s)$, when the longest ETG mode is dominant, the ZFs are already in the final,

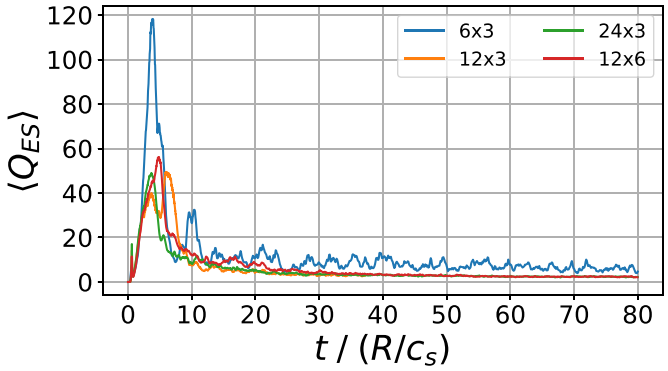

Figure 13. Convergence of the electrostatic electron heat flux for the various box size cases compared to the original $6\rho_i \times 3\rho_i$ case.

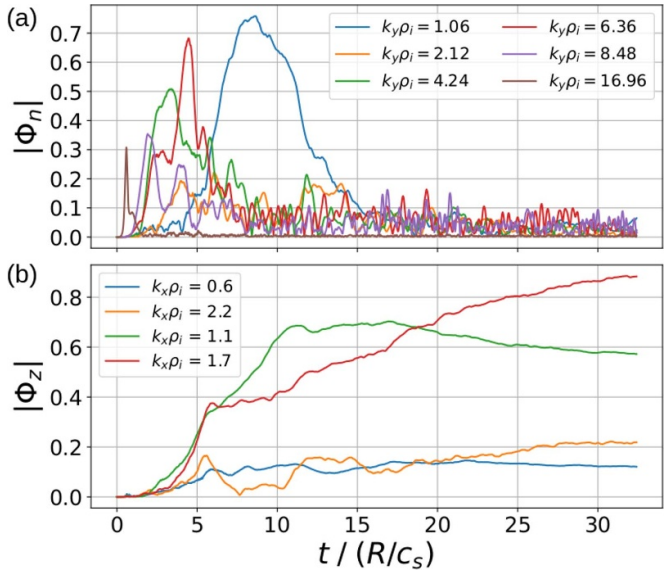

Figure 14. (*a*) ETG and (*b*) four strongest final ZF mode time traces for the $12\rho_i \times 6\rho_i$, large-y box size. All data is averaged over z.

slowly growing stage. This result indicates that the strongest ZF modes are largely being affected by the intermediate-scale ETG modes, not the longest wavelength ETG mode, and confirms the results found in section 3.2 which showed little ZF generation outside the intermediate-scale range. As increasing L_y from the original $3\rho_i$ size had no effect on the final quasi-saturated state, the largest L_x case considered, $24\rho_i \times 3\rho_i$, was chosen for the full-spectrum investigation discussed in section 4.

ORCID iDs

Stefan Tirkas https://orcid.org/0000-0002-8050-617X
Haotian Chen https://orcid.org/0000-0003-3896-4369
Gabriele Merlo https://orcid.org/0000-0003-4877-1456

References

[1] Batchelor D.A. *et al* 2007 *Plasma Sci. Technol.* **9** 312
[2] ITER Physics Expert Group on Confinement and Transport *et al* 1999 *Nucl. Fusion* **39** 2175
[3] Horton W. 1999 *Rev. Mod. Phys.* **71** 735
[4] Doyle E.J. *et al* 2007 *Nucl. Fusion* **47** S18
[5] Lee Y.C., Dong J.Q., Guzdar P.N. and Liu C.S. 1987 *Phys. Fluids* **30** 1331
[6] Jenko F., Dorland W., Kotschenreuther M. and Rogers B.N. 2000 *Phys. Plasmas* **7** 1904
[7] Dorland W., Jenko F., Kotschenreuther M. and Rogers B.N. 2000 *Phys. Rev. Lett.* **85** 5579
[8] Jenko F. and Dorland W. 2002 *Phys. Rev. Lett.* **89** 225001
[9] Nevins W.M. *et al* 2006 *Phys. Plasmas* **13** 122306
[10] Ren Y. *et al* 2017 *Nucl. Fusion* **57** 072002
[11] Gierson B.A., Stabler G.M., Solomon W.M., McKee G.R., Holland C., Austin M., Marinoni A., Schmitz L. and Pinsker R.I. 2018 *Phys. Plasmas* **25** 022509
[12] Ryter F. *et al* 2019 *Nucl. Fusion* **59** 096052
[13] Kiefer C.K., Angioni C., Tardini G., Bonanomi N., Geiger B., Mantica P., Pütterich T., Fable E. and Schneider P.A. 2021 *Nucl. Fusion* **61** 066035
[14] Howard N.T., Holland C., White A.E., Greenwald M., Candy J. and Creely A.J. 2016 *Phys. Plasmas* **23** 056109
[15] Holland C., Howard N.T. and Grierson B.A. 2017 *Nucl. Fusion* **57** 066043
[16] Parker S.E. *et al* 2006 *AIP Conf. Proc.* **871** 193
[17] Colyer G.J., Schekochihin A.A., Parra F.I., Roach C.M., Barnes M.A., Ghim Y.-C. and Dorland W. 2017 *Plasma Phys. Control. Fusion* **59** 055002
[18] Hasegawa A. and Mima K. 1977 *Phys. Rev. Lett.* **39** 205
[19] Lin Z., Chen L. and Zonca F. 2005 *Phys. Plasmas* **12** 056125
[20] Chen L., Zonca F. and Lin Z. 2005 *Plasma Phys. Control Fusion* **47** B71
[21] Kim E.J., Holland C. and Diamond P.H. 2003 *Phys. Rev. Lett.* **91** 075003
[22] Chen H., Tirkas S. and Parker S.E. 2021 *Nucl. Fusion* **61** 066017
[23] Dannert T. and Jenko F. 2005 *Phys. Plasmas* **12** 072309
[24] Jenko F. Dannert T. and Angioni C. 2005 *Plasma Phys. Control. Fusion* **47** B195
[25] Bourdelle C., Garbet X., Imbeaux F., Casati A., Dubuit N., Guirlet R. and Parisot T. 2007 *Phys. Plasmas* **14** 112501
[26] Parker S.E., Dorland W., Santoro R.A., Beer M.A., Liu Q.P., Lee W.W. and Hammett G.W. 1994 *Phys. Plasmas* **1** 1461
[27] Diamond P.H., Itoh S.-I., Itoh K. and Hahm T.S. 2005 *Plasma Phys. Control. Fusion* **47** R35
[28] Jenko F. and (The GENE development team) The GENE code (available at: https://genecode.org)
[29] Greenfield C.M., DeBoo J.C., Osborne T.H., Perkins F.W., Rosenbluth M.N. and Boucher D. 1997 *Nucl. Fusion* **37** 1215–28
[30] Dimits A.M. *et al* 2000 *Phys. Plasmas* **7** 969–83
[31] Lapillone X., Brunner S., Danner T., Jolliet S., Marinoni A., Villard L., Görler T., Jenko F. and Merz F. 2009 *Phys. Plasmas* **16** 032308
[32] Görler T., Tronko N., Hornsby W.A., Bottino A., Kleiber R., Norscini C., Grandgirard V., Jenko F. and Sonnendrücker E. 2016 *Phys. Plasmas* **23** 072503
[33] Rewoldt G., Lin Z. and Idomura Y. 2007 *Comput. Phys. Commun.* **177** 775–80
[34] Adam J.C., Tang W.M. and Rutherford P.H. 1976 *Phys. Fluids* **19** 561
[35] Chen H.-T. and Chen L. 2018 *Plasma Phys. Control. Fusion* **60** 055011
[36] Dannert T. and Jenko F. 2005 *Phys. Plasmas* **12** 072309
[37] Xiao Y. and Lin Z. 2009 *Phys. Rev. Lett.* **103** 085004
[38] Chen H. and Chen L. 2019 *Nucl. Fusion* **59** 074003
[39] Frieman R.A. and Chen L. 1982 *Phys. Fluids* **25** 502

[40] Kim J.Y. and Horton W. 1991 *Phys. Fluids* B **3** 1167
[41] Beer M.A. 1995 Gyrofluid Models of Turbulent Transport in Tokamaks *PhD Thesis* Princeton
[42] Ricci P., Rogers B.N. and Dorland W. 2010 *Phys. Plasmas* **17** 072103
[43] Strintzi D. and Jenko F. 2007 *Phys. Plasmas* **14** 042305
[44] Chen H. and Chen L. 2022 *Phys. Rev. Lett.* **128** 025003
[45] Fable E., Angioni C. and Sauter O. 2010 *Plasma Phys. Control. Fusion* **52** 015007
[46] Lapillone X., Brunner S., Sauter O., Villard L., Fable E., Görler T., Jenko F. and Merz F. 2011 *Plasma Phys. Control. Fusion* **53** 054011